ACS NANO

www.acsnano.org

ARTICLE

Programmable Anisotropy and Percolation in Supramolecular Patchy Particle Gels

Jake Song, Mehedi H. Rizvi, Brian B. Lynch, Jan Ilavsky, David Mankus, Joseph B. Tracy, Gareth H. McKinley,* and Niels Holten-Andersen*

Cite This: *ACS Nano* 2020, 14, 17018–17027

Read Online

ACCESS | Metrics & More | Article Recommendations | Supporting Information

ABSTRACT: Patchy particle interactions are predicted to facilitate the controlled self-assembly and arrest of particles into phase-stable and morphologically tunable "equilibrium" gels, which avoids the arrested phase separation and subsequent aging that is typically observed in traditional particle gels with isotropic interactions. Despite these promising traits of patchy particle interactions, such tunable equilibrium gels have yet to be realized in the laboratory due to experimental limitations associated with synthesizing patchy particles in high yield. Here, we introduce a supramolecular metal-coordination platform consisting of metallic nanoparticles linked by telechelic polymer chains, which validates the predictions associated with patchy particle interactions and facilitates the design of equilibrium particle hydrogels through limited valency interactions. We demonstrate that the interaction valency and self-assembly of the particles can be effectively controlled by adjusting the relative concentration of polymeric linkers to nanoparticles, which enables the gelation of patchy particle hydrogels with programmable local anisotropy, morphology, and low mechanical percolation thresholds. Moreover, by crowding the local environment around the patchy particles with competing interactions, we introduce an independent method to control the self-assembly of the nanoparticles, thereby enabling the design of highly anisotropic particle hydrogels with substantially reduced percolation thresholds. We thus establish a canonical platform that facilitates multifaceted control of the self-assembly of the patchy nanoparticles en route to the design of patchy particle gels with tunable valencies, morphologies, and percolation thresholds. These advances lay important foundations for further fundamental studies of patchy particle systems and for designing tunable gel materials that address a wide range of engineering applications.

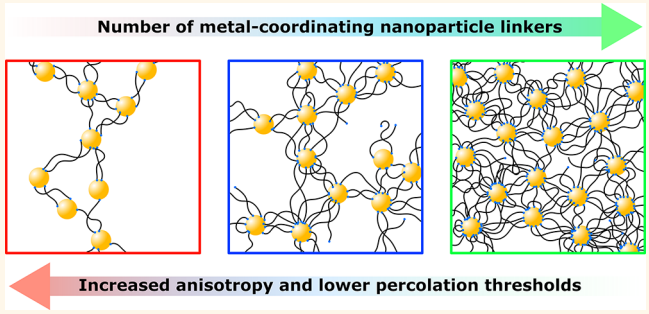

KEYWORDS: *patchy particles, self-assembly, supramolecular chemistry, equilibrium gels, bioinspired materials*

INTRODUCTION

The route to dynamic arrest in particle gels has profound consequences on their emergent structure and mechanical properties, and has important implications for understanding self-assembly in biology and optimizing the design of functional soft materials. For particles with isotropic and reversible interactions such as colloids interacting *via* depletion interactions, dynamic arrest (at volume fractions φ below the glass transition) commonly occurs through an arrested spinodal decomposition, following quenching into a two-phase coexistence region.[1,2] In contrast, for particles with limited-valency interactions, theoretical studies have predicted that arrest can occur through equilibrium associations, due to the emergence of interaction anisotropy and suppression of the two-phase region to higher interaction strength ε and lower φ (Figure 1A).[3−7] Unlike isotropic particle gels, which continuously age with time due to their underlying thermodynamic instability, these "patchy" particle gels can thus undergo "*equilibrium arrest*" and remain thermodynamically stable[7] and thus avoid temporal aging effects. Patchy particle arrest therefore represents a promising method for designing soft particle gels for materials applications requiring long-term stability, with relevance in structural and biomedical engineering. Moreover, theoretical studies have predicted that the morphology and the density of such patchy particle gels should also be tunable by controlling the valency (and therefore the anisotropy) of particle interactions,[2,6] enabling the design of stable soft materials with a broad range of microstructures. In fact,

Received: July 30, 2020
Accepted: November 16, 2020
Published: December 8, 2020

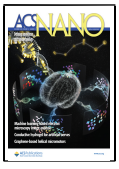

https://dx.doi.org/10.1021/acsnano.0c06389
ACS Nano 2020, 14, 17018–17027

growing evidence suggests that this exact strategy is utilized during the assembly of soft and stable biological materials with tunable microstructures, such as graded-index protein lenses in squid eyes[8] and degradation-resistant egg whites in duck eggs,[9] among others.[10,11]

Despite these promising traits of patchy particle gels, experimental validation of their properties remains limited. Although advances in molecular engineering now permit the design of a myriad of patchy particles with precise interaction sites and valencies,[12−23] these systems remain difficult to synthesize and assemble at the requisite scales for designing patchy particle gels. Thus, patchy particle arrest has so far only been studied in a narrow range of experimental systems with fixed valencies, most prominently in discotic clay particles[3] but also in molecular systems, such as DNA stars[2,7,24−26] and peptides.[27] Notably, the lack of an accessible experimental particle platform in which the particle patch valency can be tuned has prevented access to the design of gels with the wide ranges of morphologies and percolation behaviors predicted by theory.[6,8] A patchy-particle-based material system with tunable valency would not only facilitate bioinspired designs of stable particle gels with tunable morphologies and percolation thresholds[8] but also allow deeper studies of the fundamental physics of patchy particle self-assembly in a variety of environments.[2] Thus, in this work, we show that a polymer−metal nanoparticle composite gel system governed by supramolecular metal-coordination interactions[28] provides an experimental realization of a patchy particle system with tunable effective interaction valency, and permits study of the self-assembly and equilibrium arrest of particles at a variety of morphologies and percolation thresholds.

RESULTS AND DISCUSSION

Our gel system consists of 1-arm catechol-functionalized poly(ethylene glycol) (1cPEG) chains, which are grafted onto Fe_3O_4 nanoparticles (NPs), and 4-arm nitrocatechol-functionalized poly(ethylene glycol) (4nPEG) telechelic linker chains (Figure 1B). The catechol ligand coordinates strongly onto the Fe_3O_4 NP surface to facilitate a highly water-stable 1cPEG-NP complex (Figure 1C),[29] but the ligand can be dynamically exchanged by the stronger binding nitrocatechol ligand on the 4nPEG (Figure 1D).[30,31] Upon introducing the 4nPEG to an aqueous solution of 1cPEG-NP, the ligand exchange process can therefore induce bridging interactions between the initially repulsive NPs, which drives formation of a supramolecular patchy particle hydrogel (SPPH) in a state of arrest (Figure 1E).[28] As such, we may expect that the interaction valency, and thus the average coordination number M (the number of connected nearest neighbors per particle)[5,8] in the SPPH, is tunable in a straightforward manner by simply adjusting the ratio of the number of the 4nPEG linkers to the number of the NPs, $r = N_{4nPEG}/N_{NP}$. We can assume r will then be correlated to, but generally larger than, M due to the many competitive binding events that may also occur upon introducing 4nPEG linkers to the NPs. For instance, in addition to inducing high M associations between NPs, the linkers can also remain unbound, form loops (with both ends of the polymers binding to the same NPs) and form dangling ends (with one unbound end) and also multivalent interactions (with multiple linkers binding two NPs, a phenomenon which can drastically slow down dissociation).[32] These numerous possibilities and degrees of freedom make it difficult to *a priori* determine the coordination number in a patchy hydrogel system of a given linker-to-NP ratio r—this may be more feasible through simulation techniques, as demonstrated successfully in previous studies,[8,33] which would contribute to our design framework. Nevertheless, in this work, we demonstrate that this simple parameter r can adequately serve as an indirect macroscopic handle to access various phase behaviors expected from patchy particles of different interaction valencies and to design "equilibrium" gels with controlled anisotropy, morphology, and percolation behaviors.

Using prototypical concentrations of n_l = 10 wt % 4nPEG linkers and φ_{NP} = 1.93 vol % Fe_3O_4 NPs following prior work on a similar system,[28] we characterize the SPPH and test for the most distinctive hallmarks of equilibrium arrest, namely, temporal equilibration of both the mechanical and structural properties of the gel.[2−5,8,9] For a typical gel volume of V = 200 μL, these species concentrations correspond to $N_{4nPEG} = 2.0 \times 10^{-6}$ mol and $N_{NP} = 3.5 \times 10^{-8}$ mol (given $D \approx 7$ nm), thus corresponding to $r = N_{4nPEG}/N_{NP} = 10.81 n_l/\varphi_{NP} = 56$ (derivation in the Supporting Information). Time-dependent viscoelastic measurements show that, upon mixing the 4nPEG and NPs in an aqueous solution and increasing the temperature to 55 °C, gelation (as defined by the point when the storage modulus G' exceeds the loss modulus G'') is observed within 10 min (Figure S4A), followed by a steady evolution of the moduli until the moduli reach equilibrium values after approximately 8 h (Figures 1F and S4B). This gelation process is mediated by the ligand exchange and bridging of 1cPEG-NP complexes by 4nPEG (Figure 1D,E); analogous control systems with 4-arm PEGs functionalized with weaker affinity ligands that cannot displace the 1cPEG graft on the NPs as effectively are not able to create stiff gels (Figure S5). Step strain measurements of the SPPH at 25 °C reveal slow and broadly distributed stress relaxation modes, which can be succinctly captured by a Kohlrausch−Williams−Watts (KWW) model of the form $G = G_0 \exp[-(t/\tau)^{\alpha}]$, with a stretching exponent of $\alpha \approx 0.31$ (parameters in Table S3), consistent with the theoretically predicted $\alpha \approx 0.33$ for a deeply arrested equilibrium associating system (Figure 1G).[34,35] Importantly, stress relaxation measurements after 24 and 48 h of aging nearly overlap with each other, again in support of the negligible rheological aging in our patchy gel, in contrast to the substantial rheological aging observed in typical colloidal gels.[3,4] Characterization of the time-dependent structure factor $S(q)$ in the SPPH *via* small-angle X-ray scattering (SAXS) tells a similar story (Figure 1H). $S(q)$ is obtained from scattering measurements by dividing the scattered intensity $I(q)$ by a spherical form factor (Figure S7; see also Methods). A pronounced interparticle peak is observed at $q \approx 0.05$ Å (arrow in Figure 1H), corresponding to an interparticle distance of $D_{NP-NP} = 2\pi/q = 12.5$ nm, which represents the combined diameters of the particle (~7.0 nm, Figure S2B) and the bridging polymer (~5.5 nm, Figure S1B) and is in good agreement with the proposed microstructure of the SPPH (Figure 1E). The upturn in $S(q)$ at low q indicates the formation of local aggregates with fractal dimensions of D_f = 2.7 (as determined by the slope), consistent with commonly observed values in polymer gels[36,37] and biological patchy gels.[8] Characterization of $S(q)$ at even lower q *via* ultrasmall-angle X-ray scattering (USAXS) reveals that this fractal regime extends up to the local mesh size of $\xi \sim 200$ nm (Figure S6), suggesting that D_f = 2.7 originates from intramesh surface scattering of NP aggregates.[37] Importantly, unlike arrested spinodal decomposition gels which exhibit continuous structural aging with time,[1,3,4] our SPPHs exhibit no evidence of structural aging as

https://dx.doi.org/10.1021/acsnano.0c06389
ACS Nano 2020, 14, 17018−17027

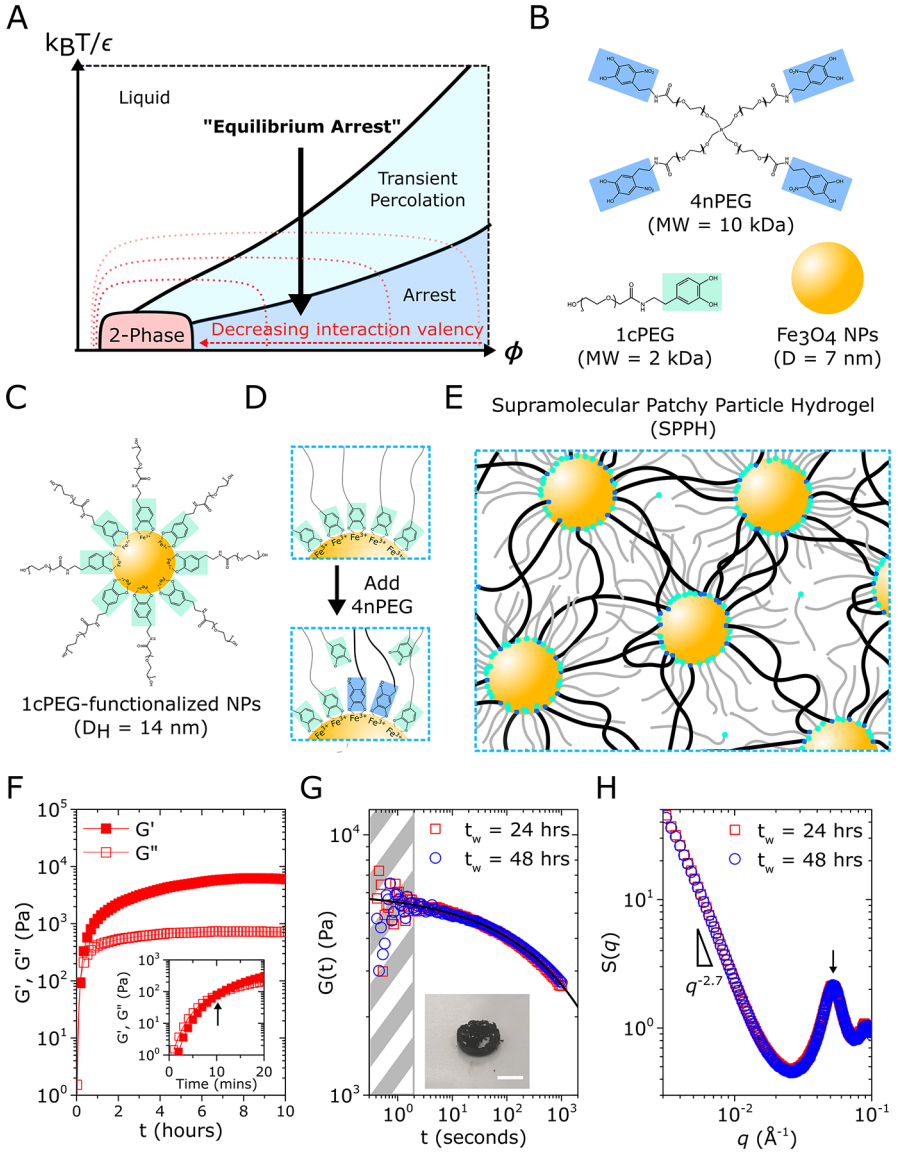

Figure 1. Design of phase-stable patchy particle hydrogels through supramolecular interactions. (A) Schematic phase diagram of attractive patchy particles as a function of effective temperature k_BT/ε and volume fractions φ. The reduction of interaction valency causes the two-phase coexistence curve to shrink to smaller φ and higher ε.[5] This contraction opens routes for patchy particles to become arrested at arbitrarily low densities through an equilibrium association−dissociation process ("equilibrium arrest") rather than an arrested spinodal decomposition.[2,35] (B) Structures of the Fe_3O_4 NPs, 1cPEG, and 4nPEG. (C) Schematic of the 1cPEG-stabilized Fe_3O_4 NP complex, which exhibits a narrow distribution in the hydrodynamic diameter around $D_H \approx 14$ nm (Figure S3C). (D) Illustration of the ligand exchange process between 1nPEG and 4nPEG that occurs at the surface of the Fe_3O_4 NP. (E) Schematic of the supramolecular patchy particle hydrogel (SPPH). Gray lines with teal caps represent 1cPEG, and black lines with blue caps represent 4nPEG linkers. (F) Time-dependent evolution of the storage modulus G' and loss modulus G'' during assembly of the SPPH system as a result of the ligand exchange process at 55 °C measured *via* small-amplitude oscillatory shear (SAOS). (Inset) Gelation, defined as the point where $G' > G''$, occurs at 10 min (arrow). (G) Relaxation modulus $G(t)$ of the SPPH at 25 °C measured at wait times of t_w = 24 h and t_w = 48 h after gelation. The solid line is a fit of the KWW equation to both sets of data. The noisy data in the shaded region at $t \leq 2$ s are within the finite response time of the instrument and are discarded from the fitting procedure. (Inset) Representative macroscopic image of the SPPH gel at r = 56. Scale bar = 1 cm. (H) Static structure factor S(q) of the SPPH (obtained by dividing the scattered intensity $I(q)$ by a spherical form factor; see Methods) at wait times of t_w = 24 h and t_w = 48 h after gelation.

manifested by the overlap in the $S(q)$ measurements after 24 and 48 h of aging, in agreement with mechanical measurements (Figure 1F,G) and providing strong evidence of equilibrium arrest in the SPPH.

Another distinct hallmark of arrested patchy particle systems is the controllability of their self-assembly and phase behavior *a priori* by the external tuning of the particle patch valency (Figure 2A).[2,5,8] We demonstrate such control in our SPPH, wherein the average coordination number M is controlled indirectly by tuning the number of 4nPEG linkers between the particles through the parameter $r = N_{4nPEG}/N_{NP}$. Through electron microscopy and rheology, we show that, at low r, the system remains in the sol state as NP self-assembly is anisotropic and sparse (due to small number of linkers); above a percolation threshold of r, the system undergoes gelation and can become progressively denser and stiffer with

https://dx.doi.org/10.1021/acsnano.0c06389
ACS Nano 2020, 14, 17018−17027

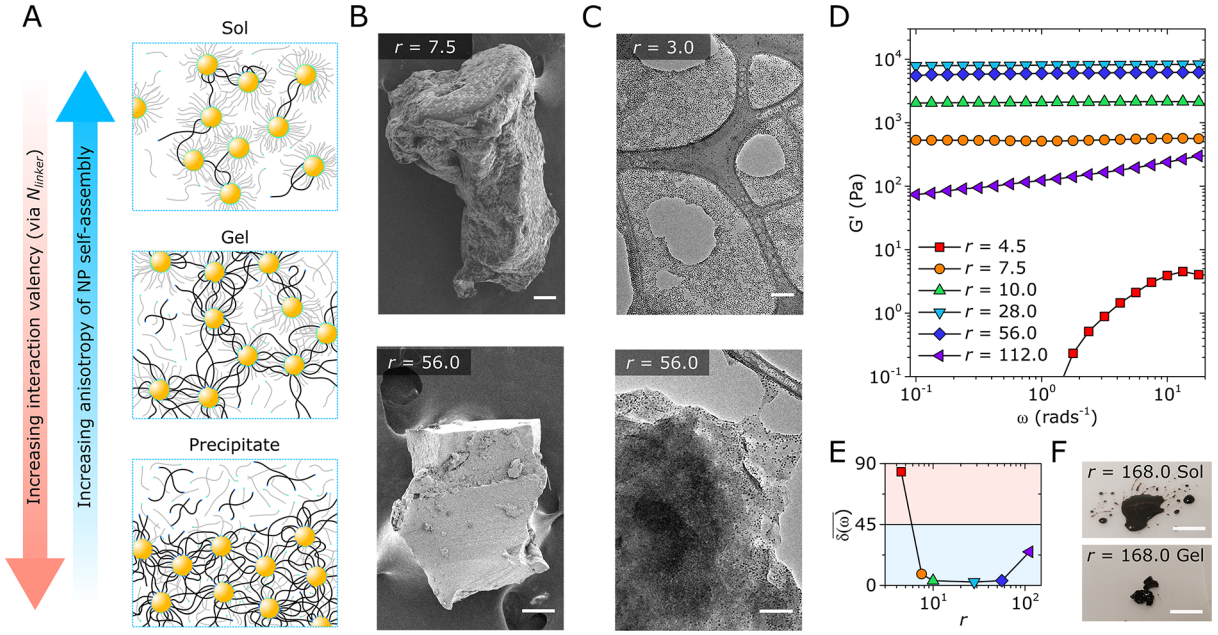

Figure 2. Systematic control of self-assembly, morphology, and rheological state behavior of the SPPH obtained by varying the linker-to-NP ratio parameter *r*. (A) Illustration of the effect of varying N_{linker} *via* the linker-to-NP ratio *r* and therefore the interaction anisotropy by introducing different amounts of 4nPEG linkers to the 1cPEG-NP complex at constant φ_{NP} and volume (same graphical representations as Figure 1E). (B) Representative SEM micrographs of the SPPH in the gel state at φ_{NP} = 1.93% and at *r* = 7.5 and *r* = 56.0. Scale bar = 100 μm. (C) Representative TEM micrographs of diluted SPPH solutions at *r* = 3.0 and *r* = 56.0. The thick strips in the micrographs are the holey carbon grids on which the samples were dried (see Methods). Scale bar = 100 nm. (D) Storage modulus $G'(\omega)$ of the SPPH at φ_{NP} = 1.93% and various *r* (corresponding rheograms of the loss modulus $G''(\omega)$ shown in Figure S10A). The viscoelastic gel state at 4.5 < *r* ≤ 56 shows an almost frequency-independent response in $G'(\omega)$ and $G''(\omega)$, consistent with the broad stress relaxation spectra observed in Figure 1G. (E) Frequency-averaged phase angle $\overline{\delta(\omega)}$ of the SPPH as a function of *r* (symbols corresponding to those in panel D). As hypothesized in panel A, increasing *r* causes the SPPH system to transition from a viscoelastic liquid (shaded in red) to a viscoelastic solid gel (shaded in blue). The onset of phase separation is observed at *r* = 112. (F) Macroscopic images of the system at *r* = 168, exhibiting visible phase separation into viscoelastic solid and viscoelastic liquid states. Scale bar = 1 cm.

increasing *r*; at higher *r*, the dense gel undergoes precipitation due to the increasing isotropy of the NP self-assembly and the expected re-emergence of the two-phase coexistence curve at high valencies (and weaker repulsive interactions) (Figure 2A).[2,5]

We demonstrate the controllability of the self-assembled microstructure of the SPPH through *r via* scanning and transmission electron microscopy (SEM/TEM). SEM microscopy images of the SPPH gels (preparation details in the Methods) show dramatic differences at *r* = 7.5, 28.0, and 56.0, with a notable increase in the extent of dark spots at lower *r* values (Figures 2B and S9A,B,E). These dark spots represent electron-density-deficient (and thus NP-deficient) regions, which is corroborated by backscattered electron micrographs of the same systems (Figure S9C,D). Thus, the SEM images provide corroboration of the expected structures of the SPPH as a function of *r* (Figure 2A). TEM images of the NP assemblies reveal the microscopic origins of these gel morphologies observed in SEM. For TEM imaging, the SPPHs were imaged in the solution state *via* significant dilution followed by air-drying on a carbon grid (see Methods). Notwithstanding the effects of the air-drying procedure on the microstructure of the system, a clear difference between the *r* = 3.0 and the *r* = 56.0 can be seen (Figures 2C and S8A,B). A sheet-like single layer of NPs is observed for *r* = 3.0, whereas NP aggregation is observed for *r* = 56.0, evidenced by the sample opacity due to lack of beam penetration. Similar NP aggregations are observed at even higher valencies facilitated by *r* = 112 (Figure S8C). We note that sheet-like layers are an important anisotropic structural motif in the SPPH—although they are not visible in the SEM micrographs discussed thus far (Figure 2B), we revisit this issue later and show that these sheet-like features do become salient and visible in SEM upon introducing a network-stabilizing competing ion. Overall, the TEM images provide microscopic evidence of the onset of anisotropy at lower *r* and *vice versa*, corroborating the different microstructures of the gels observed *via* SEM. These demonstrations of programmable morphologies in the SPPH is consistent with predicted behavior of patchy particle systems, where the interaction valency dictates the anisotropy of interactions and thus the density of the resulting self-assembled particle network.[2,3,5,6,8,9]

Rheological characterizations show that the SPPH system is able to access a wide array of rheological states, as a direct consequence of the different microstructural self-assembly of the NPs at different *r*. Linear viscoelastic measurements show that with increasing *r* at constant φ_{NP} = 1.93%, that is, with the same density of cross-linking nodes (the nanoparticles), but with varying density of linkers, the SPPH transitions from a viscoelastic fluid (*r* = 4.5) to a viscoelastic gel (4.5 < *r* ≤ 56) and then transitions back to a softer gel at higher interaction valencies (*r* = 112) (Figure 2D). This behavior is concisely illustrated by the frequency-averaged phase angle $\overline{\delta(\omega)}$ of each system: with increasing *r*, the SPPH transitions from a viscous liquid ($\overline{\delta(\omega)} \approx 90°$) to an elastic solid ($\overline{\delta(\omega)} \approx 0°$) and back toward the viscous liquid state (Figure 2E). The stiffening of the SPPH at φ_{NP} = 1.93% with increasing *r* is consistent with the expected behavior of a patchy system with varying

https://dx.doi.org/10.1021/acsnano.0c06389
ACS Nano 2020, 14, 17018−17027

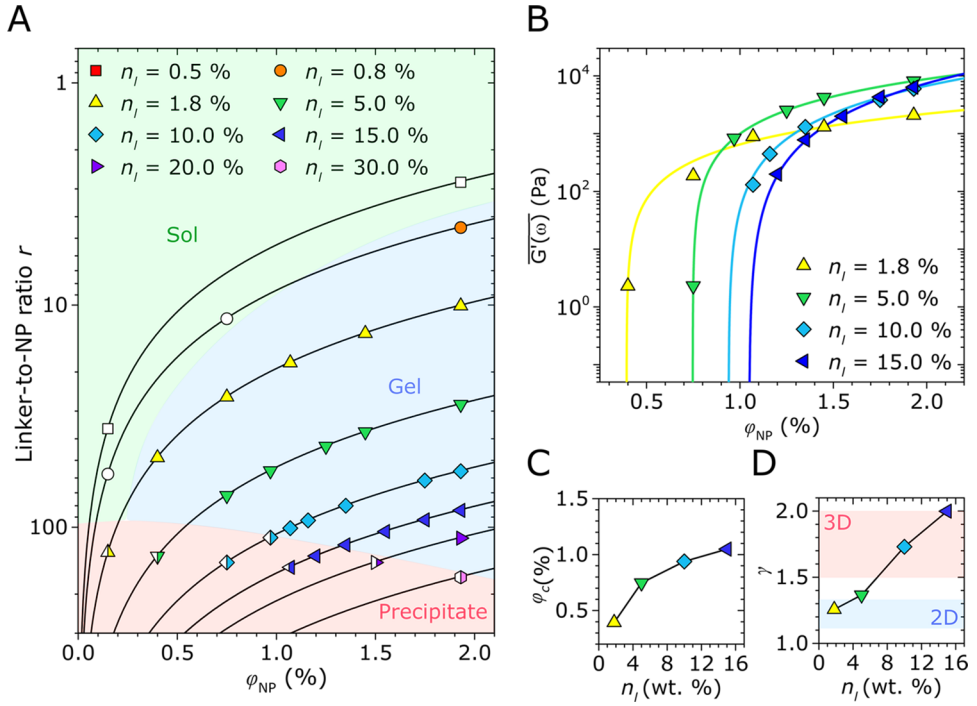

Figure 3. Systematic control of rheological states and percolation thresholds in the SPPH. (A) $r - \varphi_{NP}$ state diagram of the SPPH for different linker concentrations n_l (wt %). The state diagram is divided into sol, gel, and precipitate regions (see Figure 2A) by categorizing SPPH systems based on the following criteria: sol for systems which are visibly fluids with no observed gelation (Figure S11); gel for systems with measurable plateaus in the storage moduli $G'(\omega)$ (Figure 2D, and Figure S13); precipitate for systems which are either visibly phase-separated (see Figure 2F) or behave as fluids at the particular r but are observed to form gels at lower r. Individual sol, gel, and precipitate systems are also marked as open, filled, and half-filled symbols, respectively. The solid lines connecting the symbols represent iso-n_l lines in the $r-\varphi_{NP}$ space. Note that r is equivalent to $10.81n_l/\varphi_{NP}$ (see Supporting Information). (B) Frequency-averaged storage moduli $\overline{G'(\omega)}$ plotted as a function of φ_{NP} for SPPH with different linker concentrations n_l (wt %). Solid lines indicate fits to the percolation model $\overline{G'(\omega)} = K(\varphi - \varphi_c)^\gamma$ (fitting parameters in Table S4). (C) Percolation threshold φ_c and (D) scaling exponent γ as functions of linker concentration n_l, with symbols corresponding to the data shown in panel B. Red and blue shaded regions in (D) illustrate the range of predicted γ values *via* numerical simulations for 3-D and 2-D percolation, respectively.[36,39−41]

interaction valencies; for example, the phantom network theory shows that for a valency-controlled network with the same node density, the modulus scales with $(M - 2)/M$.[38] Re-entrant softening is observed at $r > 56$, which is indicative of an onset of phase separation due to the high interaction valency in the network; this is visibly manifested at $r = 168$, at which point the SPPH is no longer homogeneous and visibly phase separates into viscoelastic sol and gel phases (Figure 2F; rheological characterization of constituents in Figure S10B). This provides further proof that the re-entrant softening of the SPPH at $r = 112$ originates from phase separation, as expected from the emergence of the two-phase coexistence at high interaction valency.[5] The r-dependent state behaviors of the SPPH is therefore consistent with systems composed of patchy particles at different valency (Figure 1A) and suggest a direct relationship between the linker-to-NP ratio, the tunable local anisotropy, the programmable morphology of the self-assembling patchy particle network, and ultimately the final global state of the SPPH system.[2,3,5,6,8,9]

The valency-dependent rheological state behaviors of our SPPH system can be systematically explored through gelation experiments at different polymer linker concentrations n_l and NP concentrations φ_{NP}, the results of which are summarized by a state diagram of r as a function of φ_{NP} (Figure 3A). The state diagram shows that high linker-to-NP ratios r ($N_{4nPEG} \gg N_{NP}$) lead to the precipitation and collapse of the gel phase across a wide range of φ_{NP}, which is consistent with the predicted emergence of the two-phase coexistence (Figure 1A) and the densification of morphologies in the SPPH (Figure 2A−C) at high interaction valencies. Therefore, at a given linker concentration n_l, the percolation threshold for the gel phase as a function of φ_{NP} is dictated by the point at which $r = 10.81n_l/\varphi_{NP}$ is suppressed below the threshold for precipitation (roughly when the iso-n_l lines cross the $r \approx 100$ precipitate−gel boundary with increasing φ_{NP}, Figure 3A). This observation suggests that the NP percolation threshold may be tunable by adjusting the interaction valency *via* the linker concentration n_l, and indeed, rheology measurements of the SPPH across different n_l and φ_{NP} validate this hypothesis (Figures 3B and S13). The frequency-averaged storage modulus $\overline{G'(\omega)}$ is obtained by averaging $G'(\omega)$ from $\omega = 0.1$ rads^{-1} to $\omega = 42.2$ rads^{-1} for the different SPPH (full SAOS spectra in Figure S13). The mechanical percolation thresholds φ_c of the NPs of the SPPH at different n_l (Figure 3C) are obtained by fitting the data to a classic percolation model, $\overline{G'(\omega)} = K(\varphi - \varphi_c)^\gamma$, where K is a prefactor and γ is a scaling exponent related to the dimensionality of the percolating system.[36,39−41] As hypothesized, the NP percolation threshold φ_c is correlated to linker concentration n_l, in excellent agreement with the micrographs showing that low values of r drive local anisotropy in NP self-assembly and low-density SPPH morphologies (Figure 2B,C). The relationship between the scaling exponent γ and n_l tells a similar story (Figure 3D). All obtained exponents are below $\gamma \cong 2$, indicating that NP

https://dx.doi.org/10.1021/acsnano.0c06389
ACS Nano 2020, 14, 17018−17027

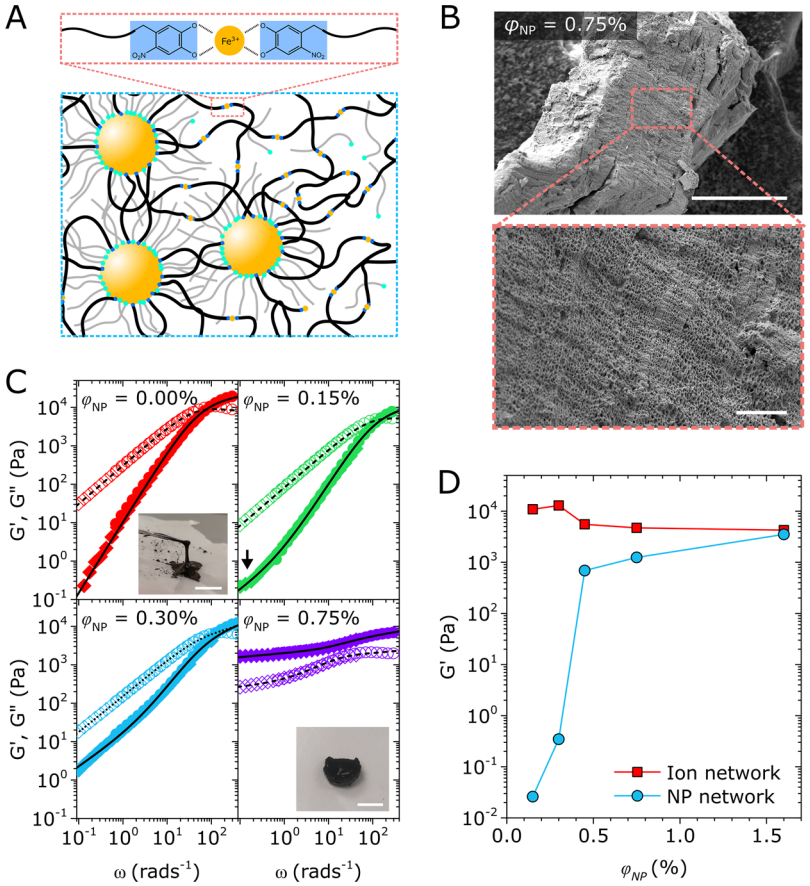

Figure 4. Independent control of the valency of particle−particle interactions in the SPPH (n_l = 10 wt %) by introducing competing interactions. (A) Schematic of the crowded SPPH with competing ion interactions (SPPH-CI). The Fe^{3+} ions introduced in the gel compete with the Fe_3O_4 NPs for the 4nPEG linkers to form difunctional coordination complexes (red box). (B) Representative SEM micrographs of the SPPH-CI system at φ_{NP} = 0.75% at different magnifications. Top panel scale bar = 100 μm; bottom panel scale bar = 10 μm. Anisotropic striations are observed throughout the sample, which are also observed in the φ_{NP} = 0.45% gel and in different samples of the φ_{NP} = 0.75% gel (Figure S16). (C) Evolution of the storage modulus $G'(\omega)$ (solid symbols) and loss modulus $G''(\omega)$ (open symbols) of the SPPH-CI with increasing φ_{NP} at 4nPEG concentrations of n_l = 10 wt % (see Figure S18C for additional φ_{NP} values). The data are obtained from SAOS measurements at 5 °C (circles) and 25 °C (diamonds) and shifted to a reference temperature of 25 °C. Solid and dashed lines indicate fits of the dynamic moduli to the FZM. The insets in the φ_{NP} = 0.00% and φ_{NP} = 0.75% panels show representative images of the SPPH-CI system at the respective NP concentrations, demonstrating a stark transition from a mobile viscoelastic liquid to a rubbery gel. Scale bar = 1 cm. (D) Elastic contributions of the Fe^{3+} ion network and the Fe_3O_4 NP network to the overall viscoelasticity of the SPPH-CI as a function of φ_{NP} based on FZM predictions (Figure S18D,E).

percolation in SPPH is analogous to percolation of resistor networks or gels with isotropic forces,[39,41] in good agreement with prior studies on polymer-bridged NPs and PEG networks.[36,40] Importantly, γ also varies systematically with n_l and decreases from $\gamma \approx 2.0$ to $\gamma \approx 1.2$ as the linker concentration is lowered from n_l = 15.0% to n_l = 1.8%. This trend is indicative of a progressive reduction in the dimensionality of the percolating system from 3-D to values close to 2-D (per numerical simulation estimates, $\gamma \approx 1.5-2.0$ for 3-D and $\gamma \approx 1.1-1.3$ for 2-D),[36,39−41] in excellent agreement with the expected onset of anisotropy at lower linker concentrations and r (Figure 2A−C). These results confirm that controlling the NP interaction valency provides programmable anisotropy, morphology, and percolation threshold of the SPPH, thus corroborating theoretical predictions[2,6,8] and advancing our ability to design structurally versatile biomimetic patchy particle systems.[8]

Lastly, we demonstrate a strategy to control the self-assembly and percolation behaviors of the SPPH independently from the aforementioned method of varying linker concentration n_l. Specifically, we hypothesized that introducing transient cross-linking species to compete with the NPs for the 4nPEG linkers may reduce the number of linkers that form between NPs, such that the asymptotic increase in r with increasing N_{4nPEG} at low φ_{NP} (Figure 3A) may be avoided. Our hypothesis is motivated by patchy particle assembly in biological settings, which often takes place in crowded viscoelastic environments such as the cellular cytosol which have many competing weak interactions.[8,42,43] Thus, to mimic such a crowded competitive macromolecular environment for the SPPH, we introduce Fe^{3+} ions to the 4nPEG linkers (n_l = 10 wt %) and NP mixture. In this configuration, the Fe^{3+} ions will compete with the Fe^{3+} ions on the Fe_3O_4 NP surface for the nitrocatechol groups in 4nPEG (thus reducing r), and form transient cross-links with the 4nPEG linkers *via* coordination bonds to form a viscoelastic fluid (Figure 4A). We refer to this system as a *supramolecular patchy particle hydrogel with competing interactions* (SPPH-CI). SEM micrographs of the SPPH-CI show that the competing ions induce striking changes in the morphology of the system compared to the SPPH. Notably, we observe highly anisotropic striations at mesoscopic length scales in the SPPH-CI *via* SEM

https://dx.doi.org/10.1021/acsnano.0c06389
ACS Nano 2020, 14, 17018−17027

(Figures 4B and S16). This shows that the SPPH-CI system is able to retain the sheet-like layers of NPs—previously observed in the regular SPPH *via* TEM (Figure 2C)—at mesoscopic length scales due to the presence of the transiently cross-linked ion network. We also observe regular porosity in the microstructure of the SPPH-CI samples, which appears to gain prominence with increasing φ_{NP} (Figure S14) and can be attributed to NP-rich domains. Lastly, TEM micrographs of the diluted SPPH-CI show clear evidence of assortative self-assembly[44] leading to a clear separation of NP-rich and ion-rich domains (Figure S15), justifying the proposed microstructure of the SPPH-CI (Figure 4A).

The onset of these highly anisotropic structures is also correlated with a much earlier onset of mechanical percolation of the NP network in the SPPH-CI compared to the regular SPPH, as demonstrated by rheological measurements of the SPPH-CI as a function of φ_{NP} for n_l = 10.0% (Figure 4C). Evidence of a contribution to the elastic modulus from the slowly relaxing NP network emerges at φ_{NP} = 0.15% (arrow), far below the critical percolation threshold of $\varphi_c \sim 0.94\%$ predicted for the regular SPPH at n_l = 10 wt % (Figure 3B,C). This finding is corroborated by the observation of an emergent NP mesostructure at φ_{NP} = 0.15% in the SPPH-CI observed *via* USAXS (Figure S17). The obvious separation of time scales between the ion and NP relaxation modes in Figure 4C allows us to capture the individual contributions of the ion and NP networks to the viscoelastic moduli *via* the fractional Zener model (FZM, Figure S18A). Fitting results to the FZM are shown as solid and dashed lines in Figure 4C, tabulated in Table S2, and shown individually in Figure S18D. This operation allows us to obtain the viscoelastic moduli of just the NP network between ω = 0.1 rads^{-1} and 42.2 rads^{-1} (*i.e.*, the dashed lines in Figure S18D) and fit the frequency-averaged moduli to the percolation model $\overline{G'(\omega)} = K(\varphi - \varphi_c)^{\gamma}$. We find that $\varphi_c \approx 0.2\%$ and $\gamma \approx 1.16$ for the NPs in the SPPH-CI (Figure S18B). These percolation parameters are lower than those from all other regular SPPHs studied, indicative of highly anisotropic self-assembly. The separation of time scales between the ion and NP relaxation modes also allows us to illustrate the individual contributions of the ion and NP components to the overall moduli of the system based on the FZM predictions in Figure S18D (Figure 4D). While the time scales for the ion and NP relaxations are estimated to be at $\omega = 10^3$ rads^{-1} and 10^{-2} rads^{-1}, respectively, we note that the trend is not sensitive to the particular ω estimates chosen for the ion and NP systems (Figure S18E). The results show that the viscoelastic response of the 4nPEG + Fe^{3+} transient network matrix dominates the overall viscoelastic response of the SPPH-CI system at low φ_{NP} (Figure 4D), which suggests that the introduced Fe^{3+} ions successfully compete for a majority of 4nPEG linkers compared to the binding sites on the NP surfaces. Therefore, competing ion interactions suppress the increase in the linker-to-NP ratio r at low φ_{NP} which would otherwise cause the collapse of the gel phase due to the high interaction valency associated with high r (Figure S19). The suppressed value of the ratio r also facilitates a highly anisotropic and low-density self-assembly of NPs, in agreement with our earlier hypothesis. These findings highlight the potentially complementary role of crowding and competition in facilitating anisotropic self-assembly of patchy building blocks in biology[8,9,42] and provides a bioinspired approach to independently tailor the interaction valency, morphology, and density of patchy particle assemblies in engineered soft materials.

CONCLUSION

We have presented a supramolecular polymer-bridged patchy particle hydrogel system that can serve as an experimental platform for designing particle gels which not only are phase-stable but also offer tunability in the particle−particle interaction valency, thus providing access to a wide range of morphologies and percolation behaviors that have been predicted by theory. We show that the valency of the particle−particle interaction can be effectively tuned by adjusting the number of polymer linkers per particle and also independently by adding competing interactions to the system. The precise quantitative relation between r and the coordination number M remains unclear; however, we anticipate that additional simulations would provide critical insight into the M of the SPPH and facilitate greater rational control over the design of the anisotropic supramolecular hydrogels. Beyond our SPPH system, we expect the findings in this work to be salient for a wide range of gel systems with controllable cross-link functionalities, such as DNA gels,[24] metal−organic cage gels,[33] protein gels,[8,11] bridged particle gels,[36,45−51] and multifunctional polymer gels.[52] We anticipate these findings will accelerate the design of bioinspired programmable soft materials for structural and biomedical applications and inspire deeper studies of the physics of patchy particle self-assembly in diverse environments.

METHODS

Polymer Synthesis. Unless specifically stated otherwise, all chemicals are purchased from Sigma-Aldrich. The 4-arm PEG *N*-hydrosuccinimide (10 kDa, JenKem Technology) was functionalized with nitrocatechol using a variation of previously reported methods to create 4-arm nitrocatechol PEG (4nPEG).[53] Nitrodopamine end-groups were first synthesized by dissolving 1.00 g of dopamine hydrochloride and 1.45 g of sodium nitrite in 30 mL of water. The reaction vessel was then placed into an ice bath, and 5.0 mL of 20% w/w sulfuric acid was slowly added under vigorous stirring. The yellow precipitate was collected through vacuum filtration, washed with cold water once and cold methanol three times, and vacuum-dried. The 4-arm PEG *N*-hydrosuccinimide was then functionalized with the collected nitrodopamine salt by dissolving 1.0 g of 4-arm PEG *N*-hydrosuccinimide and 0.24 g of the nitrodopamine salt (2× equivalent of *N*-hydrosuccinimide) in 12 mL of DMF. The reaction vessel was then moved to an oil bath at 55 °C, and 0.2 mL of TEA (>2× equivalent of *N*-hydrosuccinimide) was added to initiate the coupling. The reaction was left to proceed under N_2 overnight. Afterward, the product was extracted with chloroform and dried using sodium sulfate. The product was then precipitated in diethyl ether three times and vacuum-dried. The functional efficiency of the 4nPEG was typically around ∼88% (see Calculations section in the Supplementary Information).

The 1-arm PEG *N*-hydrosuccinimide (2 kDa, JenKem Technology) and 4-arm PEG *N*-hydrosuccinimide (10 kDa, JenKem Technology) were functionalized with catechol to create 1-arm catechol PEG (1cPEG) and 4-arm catechol PEG (4cPEG) following the same method but without the conversion step from dopamine to nitrodopamine.

Nanoparticle Synthesis. Oleylamine-stabilized Fe_3O_4 NPs with an average diameter of 7 nm were synthesized by reductive decomposition of an iron salt in a heat-up method.[54,55] In a typical synthesis, 1.05 g of iron(III) acetylacetonate (99%, Strem Chemicals) was dissolved in a mixture of 15 mL of benzyl ether (99%, Acros Organics) and 15 mL of oleylamine (98%) in a 100 mL, three-necked, round-bottomed flask. Oleylamine serves as both the reducing agent

https://dx.doi.org/10.1021/acsnano.0c06389
ACS Nano 2020, 14, 17018−17027

and stabilizing ligand. The mixture was vigorously stirred and degassed under vacuum at room temperature for 1 h, followed by heating (ramp rate of ∼7 °C/min) at 120 °C for 1 h. During the temperature ramp, the flask was backfilled with nitrogen at 90 °C. The mixture was then quickly heated under inert atmosphere to 210 °C (heating rate of ∼15 °C/min) and held for 1 h. Upon cooling to 50 °C, 50 mL of ethanol was added to the dark brown reaction product, followed by subsequent centrifugation and redispersion in THF. The oleylamine-functionalized Fe_3O_4 NPs dispersed in THF were then functionalized with 1cPEG by adding 1cPEG to the mixture at a 1cPEG/Fe_3O_4 mass ratio of 3:1. The mixture was heated to 55 °C, and ligand exchange was allowed to proceed for 24 h. The resulting solution was then precipitated in hexane three times before being dried under vacuum.

SPPH Gel Synthesis. SPPH gels are made by mixing aqueous solutions of 4nPEG, 1cPEG-NP, and HCl to make a final volume of 200 μL and pH of ∼2.2, with varying amounts of 4nPEG and 1cPEG-NP depending on the n_l and φ_{NP} (note that φ_{NP} is defined with respect to the volume of the Fe_3O_4 core, not the entire 1cPEG-NP complex). An acidic environment for the SPPH is chosen due to the fact that a pH of ∼2 facilitates stable mono-coordinations between nitrocatechol and iron on the Fe_3O_4 surface.[56] At higher pH of ∼5.2, where affinities are stronger and bis-coordinations dominate,[56] we found that the NPs showed some signs of etching, manifested by an emergence of an Fe^{3+} ion relaxation mode even in the absence of Fe^{3+} ions added (Figure S20). Therefore, an acidic environment is used to prevent any trace amounts of Fe^{3+} ions in the 1cPEG-NP solution from participating in the cross-linking of the gel. SPPH with competing ions (SPPH-CI) are made by mixing aqueous solutions of 4nPEG, 1cPEG-NP, $FeCl_3$ (added with a stoichiometric ratio of 2 nitrocatechol to 1 Fe^{3+}), and NaAc buffer to make a final volume of 200 μL and a pH of ∼5.2 to facilitate bis-coordinations (Figure 4A). Although the etching effect found in the regular SPPH at this pH will likely contribute to an increased availability of Fe^{3+} beyond the stoichiometric amount added, this does not affect the gelation of the system,[56] and the etching effect on the size of the NPs was negligible, as indicated by USAXS scattering intensities of the SPPH-CI compared to the regular SPPH (Figure S17 and Table S1). For a typical sample, the mixture is sealed and placed in a 55 °C oven for 24 h to create a gel.

Nuclear Magnetic Resonance. ^{1}H spectra of 4nPEG were obtained using a Varian 300 MHz spectrometer on a 4nPEG sample dissolved in $CDCl_3$ (10 mg/mL).

Dynamic Light Scattering (DLS). DLS measurements were made using an Anton-Paar Litesizer 100 particle size analyzer. The number-weighted size distribution of 4nPEGs (Figure S1B) was obtained on samples at 10 wt % dilutions in water. The number-weighted size distribution of 1cPEG-functionalized NPs (Figure S3C) were obtained on much more diluted samples (0.01 wt %) due to the black opaque color of the specimen. Measurements were repeated three times to ensure reproducibility of data.

Thermogravimetric Analysis (TGA). Mass profiles of dry 1cPEG-functionalized Fe_3O_4 NPs were characterized using a TA Instruments Q500 TGA. After equilibration at 25 °C, the oven temperature was ramped to 500 °C at 10 °C/min under nitrogen gas flow rates of 60 mL/min.

Scanning Electron Microscopy. All SEM images were obtained using a Zeiss Crossbeam 540 field-emission SEM operating at 3−9 kV using currents ranging from 500 to 1000 pA. Unless stated otherwise, all images were obtained *via* secondary electron scattering mode. Prior to imaging, samples were chemically fixed with glutaraldehyde—a broadly reactive molecule commonly used to fix biological samples due to its ability to cross-link amine and hydroxyl groups. The samples are then dried using tetramethylsilane (TMS) to preserve as much of the hydrated morphology as possible under high vacuum.[57,58] To do so, hydrated specimens were first fixed in 2% glutaraldehyde and then dehydrated by substituting water with a series of ethanol concentrations (35, 45, 55, 65, 75, 85, 95, and 100%). The specimens were then transitioned through gradations of ethanol and TMS (50%/50%, 20%/80%, and 100% TMS) and then allowed to air-dry under the fume hood. Although this fixation and drying procedure caused affine shrinkages to the sample, salient microstructural elements were retained after the fixation and drying steps, allowing for qualitative but informative imaging of the gels in their native state (Figure S21).

Transmission Electron Microscopy. TEM images of the NPs were obtained using a FEI Talos F200X G2. Samples were prepared by dispersing Fe_3O_4 NPs in hexane and then dropping a diluted solution onto a TEM grid. The size distribution of the NPs was obtained through pixel analysis of the images *via* ImageJ. TEM images of the SPPHs were obtained using a FEI Tecnai G2 Spirit Twin TEM operating at 120 kV. Samples were prepared by synthesizing the SPPHs at 1/1000 the original concentration. This diluted solution was then dropped and air-dried onto 200 mesh carbon-coated copper holey grids from Ted-Pella, as the holes allow for imaging of the organic PEG phase.

Ultrasmall-Angle X-ray Scattering. USAXS and SAXS intensities were collected using the USAXS instrument at 9-ID beamline at the Advanced Photon Source (APS). Samples were mounted in cells with a sample thickness of ∼1 mm and with 3M Scotch tape on either side. Due to variations in the thickness of the actual samples, only relative intensities are reported in the paper. X-ray energy was 21 keV (wavelength = 0.5905 Å), and the beam size was 0.6 × 0.6 mm for USAXS and 0.1 × 0.6 mm for SAXS. Data collection was 90 s for USAXS and 15 s for SAXS. Data were subtracted from a blank cell with Scotch tape, reduced, and then merged together using software (Indra, Nika, and Irena) provided by the beamline.[59,60] Slit smearing inherent to the USAXS instrument was removed using desmearing routines in Irena to generate pinhole equivalent data for analysis.

Time-Dependent Small-Angle X-ray Scattering. Time-dependent SAXS measurements were carried out using a pinhole camera at the small-angle XPCS beamline 8-ID-I at the APS. Samples were mounted in cells with a sample thickness of 1.5 mm and were sealed with thin polycarbonate windows on either side. Due to variations in the thickness of the actual samples, only relative small-angle scattering intensities are reported in the paper. Monochromatic X-rays at an energy of 7.35 keV were used, and the beam size was 15 μm × 15 μm, with a nominal flux of 10^9 photons/s, which is then attenuated by a factor of 14. A large area medipix based detector array (LAMBDA) with a pixel size of 55 μm and array size of 516 × 1556 was used. The measurements were checked for radiation damage by controlling the dose using filters, and an optimum dose was determined for the measurements.

Linear Rheology. All viscoelastic measurements of the hydrogels were conducted using Anton-Paar's MCR-302 stress-controlled rheometer, with a 10 mm parallel plate geometry and a gap size of 1 mm. All gels were loaded, trimmed, and sealed with mineral oil prior to characterization to prevent dehydration. Time-dependent small-amplitude oscillatory shear (SAOS) experiments for gelation measurements in Figure 1F were conducted at an angular frequency ω = 5 rads^{-1} at an amplitude of γ = 1%. All other SAOS experiments were conducted at an amplitude of γ = 1%. Step strain experiments for relaxation measurements in Figure 1G were conducted at an amplitude of γ = 1%. Large amplitude oscillatory shear measurements were conducted at an angular frequency ω = 5 rads^{-1} to ensure that γ = 1% is within the linear regime (Figure S4C).

ASSOCIATED CONTENT

Supporting Information

The Supporting Information is available free of charge at https://pubs.acs.org/doi/10.1021/acsnano.0c06389.

Fitting parameters, calculation and analysis schemes, NMR/DLS characterization of polymers and nanoparticles, and supplementary rheological data, scattering curves, and microscopy images of the SPPH and SPPH-CI systems (PDF)

https://dx.doi.org/10.1021/acsnano.0c06389
ACS Nano 2020, 14, 17018−17027

AUTHOR INFORMATION

Corresponding Authors

Gareth H. McKinley − *Department of Mechanical Engineering, Massachusetts Institute of Technology, Cambridge, Massachusetts 02139, United States;* orcid.org/0000-0001-8323-2779; Email: gareth@mit.edu

Niels Holten-Andersen − *Department of Materials Science and Engineering, Massachusetts Institute of Technology, Cambridge, Massachusetts 02139, United States;* orcid.org/0000-0002-5318-9674; Email: holten@mit.edu

Authors

Jake Song − *Department of Mechanical Engineering and Department of Materials Science and Engineering, Massachusetts Institute of Technology, Cambridge, Massachusetts 02139, United States;* orcid.org/0000-0003-1254-6206

Mehedi H. Rizvi − *Department of Materials Science and Engineering, North Carolina State University, Raleigh, North Carolina 27695, United States*

Brian B. Lynch − *Department of Materials Science and Engineering, North Carolina State University, Raleigh, North Carolina 27695, United States;* orcid.org/0000-0002-4407-4541

Jan Ilavsky − *X-ray Science Division at the Advanced Photon Source, Argonne National Laboratory, Lemont, Illinois 60439, United States;* orcid.org/0000-0003-1982-8900

David Mankus − *Koch Institute for Integrative Cancer Research, Massachusetts Institute of Technology, Cambridge, Massachusetts 02139, United States*

Joseph B. Tracy − *Department of Materials Science and Engineering, North Carolina State University, Raleigh, North Carolina 27695, United States;* orcid.org/0000-0002-3358-3703

Complete contact information is available at: https://pubs.acs.org/10.1021/acsnano.0c06389

Author Contributions

J.S., G.H.M., and N.H.-A. designed the study and interpreted the results, M.H.R. and B.B.L. synthesized and characterized nanoparticles. J.S. and J.I. performed USAXS characterization and analysis. J.S. and D.M. performed SEM characterization and analysis. J.S. performed all other experimental procedures. J.S., G.H.M., and N.H.-A. drafted the manuscript with input from J.B.T. as well as all other authors. G.H.M. and N.H.-A. co-supervised the study.

Notes

The authors declare no competing financial interest.

ACKNOWLEDGMENTS

J.S. would like to thank H. Le Roy, M. Lenz (Paris-Sud), J.F. Douglas (NIST), and S. Kumar (Columbia) for helpful discussions, and I. Kuzmenko, S. Narayanan, Q. Zhang (ANL), C. Viry, and C. McCue (MIT) for assistance with USAXS, SAXS, TGA, and DLS, respectively. The authors acknowledge instrumental access from the Advanced Photon Source (APS), a U.S. Department of Energy (DOE) Office of Science User Facility operated for the DOE Office of Science by Argonne National Laboratory under Contract No. DE-AC02-06CH11357. The authors acknowledge instrumental access from the Swanson Biotechnology Center at the Koch Institute at MIT. The authors acknowledge instrumental access from the Analytical Instrumentation Facility (AIF) at North Carolina State University, which is supported by the State of North Carolina and the National Science Foundation (EECS-2025064). The authors acknowledge financial support from the U.S. Army Research Office through the Institute for Soldier Nanotechnologies at MIT under Contract No. W911NF-13-D-0001, and the National Science Foundation through the research Grant Nos. CBET-1605943 and CBET-1605699 as well as the MIT Materials Research Science and Engineering Center grant DMR-1419807. J.S. acknowledges financial support from the MIT Presidential Fellowship.

REFERENCES

(1) Lu, P. J.; Zaccarelli, E.; Ciulla, F.; Schofield, A. B.; Sciortino, F.; Weitz, D. A. Gelation of Particles with Short-Range Attraction. *Nature* **2008**, *453* (7194), 499.

(2) Sciortino, F.; Zaccarelli, E. Equilibrium Gels of Limited Valence Colloids. *Curr. Opin. Colloid Interface Sci.* **2017**, *30*, 90−96.

(3) Ruzicka, B.; Zaccarelli, E.; Zulian, L.; Angelini, R.; Sztucki, M.; Moussaïd, A.; Narayanan, T.; Sciortino, F. Observation of Empty Liquids and Equilibrium Gels in a Colloidal Clay. *Nat. Mater.* **2011**, *10* (1), 56.

(4) Zaccarelli, E. Colloidal Gels: Equilibrium and Non-Equilibrium Routes. *J. Phys.: Condens. Matter* **2007**, *19* (32), 323101.

(5) Bianchi, E.; Largo, J.; Tartaglia, P.; Zaccarelli, E.; Sciortino, F. Phase Diagram of Patchy Colloids: Towards Empty Liquids. *Phys. Rev. Lett.* **2006**, *97* (16), 168301.

(6) Russo, J.; Tartaglia, P.; Sciortino, F. Reversible Gels of Patchy Particles: Role of the Valence. *J. Chem. Phys.* **2009**, *131* (1), No. 014504.

(7) Rovigatti, L.; Smallenburg, F.; Romano, F.; Sciortino, F. Gels of DNA Nanostars Never Crystallize. *ACS Nano* **2014**, *8* (4), 3567−3574.

(8) Cai, J.; Townsend, J. P.; Dodson, T. C.; Heiney, P. A.; Sweeney, A. M. Eye Patches: Protein Assembly of Index-Gradient Squid Lenses. *Science* **2017**, *357* (6351), 564−569.

(9) Cai, J.; Sweeney, A. M. The Proof Is in the Pidan: Generalizing Proteins as Patchy Particles. *ACS Cent. Sci.* **2018**, *4* (7), 840−853.

(10) McManus, J. J.; Charbonneau, P.; Zaccarelli, E.; Asherie, N. The Physics of Protein Self-Assembly. *Curr. Opin. Colloid Interface Sci.* **2016**, *22*, 73−79.

(11) Roosen-Runge, F.; Zhang, F.; Schreiber, F.; Roth, R. Ion-Activated Attractive Patches as a Mechanism for Controlled Protein Interactions. *Sci. Rep.* **2015**, *4*, 7016.

(12) Jiang, S.; Chen, Q.; Tripathy, M.; Luijten, E.; Schweizer, K. S.; Granick, S. Janus Particle Synthesis and Assembly. *Adv. Mater.* **2010**, *22* (10), 1060−1071.

(13) Zhang, J.; Luijten, E.; Granick, S. Toward Design Rules of Directional Janus Colloidal Assembly. *Annu. Rev. Phys. Chem.* **2015**, *66*, 581−600.

(14) Wang, Y.; Wang, Y.; Breed, D. R.; Manoharan, V. N.; Feng, L.; Hollingsworth, A. D.; Weck, M.; Pine, D. J. Colloids with Valence and Specific Directional Bonding. *Nature* **2012**, *491* (7422), 51.

(15) Wang, Y.; Hollingsworth, A. D.; Yang, S. K.; Patel, S.; Pine, D. J.; Weck, M. Patchy Particle Self-Assembly *via* Metal Coordination. *J. Am. Chem. Soc.* **2013**, *135* (38), 14064−14067.

(16) Yi, G.-R.; Pine, D. J.; Sacanna, S. Recent Progress on Patchy Colloids and Their Self-Assembly. *J. Phys.: Condens. Matter* **2013**, *25* (19), 193101.

(17) Sacanna, S.; Korpics, M.; Rodriguez, K.; Colón-Meléndez, L.; Kim, S.-H.; Pine, D. J.; Yi, G.-R. Shaping Colloids for Self-Assembly. *Nat. Commun.* **2013**, *4*, 1688.

(18) Sacanna, S.; Pine, D. J.; Yi, G.-R. Engineering Shape: The Novel Geometries of Colloidal Self-Assembly. *Soft Matter* **2013**, *9* (34), 8096−8106.

(19) Diaz A, J. A.; Oh, J. S.; Yi, G.-R.; Pine, D. J. Photo-Printing of Faceted DNA Patchy Particles. *Proc. Natl. Acad. Sci. U. S. A.* **2020**, *117* (20), 10645−10653.
(20) Gong, Z.; Hueckel, T.; Yi, G.-R.; Sacanna, S. Patchy Particles Made by Colloidal Fusion. *Nature* **2017**, *550* (7675), 234−238.
(21) Hueckel, T.; Sacanna, S. Mix-and-Melt Colloidal Engineering. *ACS Nano* **2018**, *12* (4), 3533−3540.
(22) Glotzer, S. C.; Solomon, M. J. Anisotropy of Building Blocks and Their Assembly into Complex Structures. *Nat. Mater.* **2007**, *6* (8), 557.
(23) Hermans, T. M.; Broeren, M. A.; Gomopoulos, N.; Van Der Schoot, P.; Van Genderen, M. H.; Sommerdijk, N. A.; Fytas, G.; Meijer, E. Self-Assembly of Soft Nanoparticles with Tunable Patchiness. *Nat. Nanotechnol.* **2009**, *4* (11), 721.
(24) Biffi, S.; Cerbino, R.; Bomboi, F.; Paraboschi, E. M.; Asselta, R.; Sciortino, F.; Bellini, T. Phase Behavior and Critical Activated Dynamics of Limited-Valence DNA Nanostars. *Proc. Natl. Acad. Sci. U. S. A.* **2013**, *110* (39), 15633−15637.
(25) Fernandez-Castanon, J.; Bomboi, F.; Rovigatti, L.; Zanatta, M.; Paciaroni, A.; Comez, L.; Porcar, L.; Jafta, C. J.; Fadda, G. C.; Bellini, T.; Sciortino, F. Small-Angle Neutron Scattering and Molecular Dynamics Structural Study of Gelling DNA Nanostars. *J. Chem. Phys.* **2016**, *145* (8), No. 084910.
(26) Spinozzi, F.; Ortore, M. G.; Nava, G.; Bomboi, F.; Carducci, F.; Amenitsch, H.; Bellini, T.; Sciortino, F.; Mariani, P. Gelling without Structuring: A Saxs Study of the Interactions among DNA Nanostars. *Langmuir* **2020**, *36* (35), 10387−10396.
(27) Dudukovic, N. A.; Zukoski, C. F. Evidence for Equilibrium Gels of Valence-Limited Particles. *Soft Matter* **2014**, *10* (39), 7849−7856.
(28) Li, Q.; Barrett, D. G.; Messersmith, P. B.; Holten-Andersen, N. Controlling Hydrogel Mechanics *via* Bio-Inspired Polymer−Nanoparticle Bond Dynamics. *ACS Nano* **2016**, *10* (1), 1317−1324.
(29) Xie, J.; Xu, C.; Kohler, N.; Hou, Y.; Sun, S. Controlled Pegylation of Monodisperse Fe3o4 Nanoparticles for Reduced Non-Specific Uptake by Macrophage Cells. *Adv. Mater.* **2007**, *19* (20), 3163−3166.
(30) Cencer, M.; Murley, M.; Liu, Y.; Lee, B. P. Effect of Nitro-Functionalization on the Cross-Linking and Bioadhesion of Biomimetic Adhesive Moiety. *Biomacromolecules* **2015**, *16* (1), 404−410.
(31) Amstad, E.; Gehring, A. U.; Fischer, H.; Nagaiyanallur, V. V.; Hähner, G.; Textor, M.; Reimhult, E. Influence of Electronegative Substituents on the Binding Affinity of Catechol-Derived Anchors to Fe3o4 Nanoparticles. *J. Phys. Chem. C* **2011**, *115* (3), 683−691.
(32) Huskens, J.; Prins, L. J.; Haag, R.; Ravoo, B. J. *Multivalency: Concepts, Research and Applications*, 1st ed.; John Wiley & Sons: Hoboken, NJ, 2018; pp 23−68.
(33) Zhukhovitskiy, A. V.; Zhong, M.; Keeler, E. G.; Michaelis, V. K.; Sun, J. E.; Hore, M. J.; Pochan, D. J.; Griffin, R. G.; Willard, A. P.; Johnson, J. A. Highly Branched and Loop-Rich Gels *via* Formation of Metal−Organic Cages Linked by Polymers. *Nat. Chem.* **2016**, *8* (1), 33.
(34) Stukalin, E. B.; Douglas, J. F.; Freed, K. F. Multistep Relaxation in Equilibrium Polymer Solutions: A Minimal Model of Relaxation in "Complex" Fluids. *J. Chem. Phys.* **2008**, *129* (9), No. 094901.
(35) Kumar, S. K.; Douglas, J. F. Gelation in Physically Associating Polymer Solutions. *Phys. Rev. Lett.* **2001**, *87* (18), 188301.
(36) Surve, M.; Pryamitsyn, V.; Ganesan, V. Universality in Structure and Elasticity of Polymer-Nanoparticle Gels. *Phys. Rev. Lett.* **2006**, *96* (17), 177805.
(37) Malo de Molina, P.; Lad, S.; Helgeson, M. E. Heterogeneity and Its Influence on the Properties of Difunctional Poly (Ethylene Glycol) Hydrogels: Structure and Mechanics. *Macromolecules* **2015**, *48* (15), 5402−5411.
(38) Rubinstein, M.; Colby, R. H. *Polymer Physics*; Oxford University Press: New York, 2003; Vol. *23*.
(39) De Gennes, P.-G. On a Relation between Percolation Theory and the Elasticity of Gels. *J. Phys., Lett.* **1976**, *37* (1), 1−2.
(40) Nishi, K.; Fujii, K.; Chung, U.-i.; Shibayama, M.; Sakai, T. Experimental Observation of Two Features Unexpected from the Classical Theories of Rubber Elasticity. *Phys. Rev. Lett.* **2017**, *119* (26), 267801.
(41) Kirkpatrick, S. Percolation and Conduction. *Rev. Mod. Phys.* **1973**, *45* (4), 574.
(42) Bucciarelli, S.; Myung, J. S.; Farago, B.; Das, S.; Vliegenthart, G. A.; Holderer, O.; Winkler, R. G.; Schurtenberger, P.; Gompper, G.; Stradner, A. Dramatic Influence of Patchy Attractions on Short-Time Protein Diffusion under Crowded Conditions. *Science Advances* **2016**, *2* (12), No. e1601432.
(43) Berret, J.-F. Local Viscoelasticity of Living Cells Measured by Rotational Magnetic Spectroscopy. *Nat. Commun.* **2016**, *7*, 10134.
(44) Newman, M. E. Assortative Mixing in Networks. *Phys. Rev. Lett.* **2002**, *89* (20), 208701.
(45) Zhang, W.; Travitz, A.; Larson, R. G. Modeling Intercolloidal Interactions Induced by Adsorption of Mobile Telechelic Polymers onto Particle Surfaces. *Macromolecules* **2019**, *52* (14), 5357−5365.
(46) Choudhury, S.; Mangal, R.; Agrawal, A.; Archer, L. A. A Highly Reversible Room-Temperature Lithium Metal Battery Based on Crosslinked Hairy Nanoparticles. *Nat. Commun.* **2015**, *6* (1), 10101.
(47) Appel, E. A.; Tibbitt, M. W.; Webber, M. J.; Mattix, B. A.; Veiseh, O.; Langer, R. Self-Assembled Hydrogels Utilizing Polymer−Nanoparticle Interactions. *Nat. Commun.* **2015**, *6*, 6295.
(48) Jaiswal, M. K.; Xavier, J. R.; Carrow, J. K.; Desai, P.; Alge, D.; Gaharwar, A. K. Mechanically Stiff Nanocomposite Hydrogels at Ultralow Nanoparticle Content. *ACS Nano* **2016**, *10* (1), 246−256.
(49) Wang, Q.; Mynar, J. L.; Yoshida, M.; Lee, E.; Lee, M.; Okuro, K.; Kinbara, K.; Aida, T. High-Water-Content Mouldable Hydrogels by Mixing Clay and a Dendritic Molecular Binder. *Nature* **2010**, *463* (7279), 339.
(50) Yu, A. C.; Chen, H.; Chan, D.; Agmon, G.; Stapleton, L. M.; Sevit, A. M.; Tibbitt, M. W.; Acosta, J. D.; Zhang, T.; Franzia, P. W.; Langer, R.; Appel, E. A. Scalable Manufacturing of Biomimetic Moldable Hydrogels for Industrial Applications. *Proc. Natl. Acad. Sci. U. S. A.* **2016**, *113* (50), 14255−14260.
(51) Zhou, Y.; Damasceno, P. F.; Somashekar, B. S.; Engel, M.; Tian, F.; Zhu, J.; Huang, R.; Johnson, K.; McIntyre, C.; Sun, K.; Yang, M.; Green, P. F.; Ramamoorthy, A.; Glotzer, S. C.; Kotov, N. A. Unusual Multiscale Mechanics of Biomimetic Nanoparticle Hydrogels. *Nat. Commun.* **2018**, *9* (1), 181.
(52) Feldman, K. E.; Kade, M. J.; Meijer, E.; Hawker, C. J.; Kramer, E. J. Model Transient Networks from Strongly Hydrogen-Bonded Polymers. *Macromolecules* **2009**, *42* (22), 9072−9081.
(53) Shafiq, Z.; Cui, J.; Pastor-Pérez, L.; San Miguel, V.; Gropeanu, R. A.; Serrano, C.; del Campo, A. Bioinspired Underwater Bonding and Debonding on Demand. *Angew. Chem.* **2012**, *124* (18), 4408−4411.
(54) Xu, Z.; Shen, C.; Hou, Y.; Gao, H.; Sun, S. Oleylamine as Both Reducing Agent and Stabilizer in a Facile Synthesis of Magnetite Nanoparticles. *Chem. Mater.* **2009**, *21* (9), 1778−1780.
(55) Chapman, B. S.; Wu, W.-C.; Li, Q.; Holten-Andersen, N.; Tracy, J. B. Heteroaggregation Approach for Depositing Magnetite Nanoparticles onto Silica-Overcoated Gold Nanorods. *Chem. Mater.* **2017**, *29* (24), 10362−10368.
(56) Cazzell, S. A.; Holten-Andersen, N. Expanding the Stoichiometric Window for Metal Cross-Linked Gel Assembly Using Competition. *Proc. Natl. Acad. Sci. U. S. A.* **2019**, *116* (43), 21369−21374.
(57) Reville, W. J.; Heapes, M. M.; O'Sullivan, V. R. A Survey to Assess the Ultrastructural Preservation of Fixed Biological Samples after Air-Drying from Tetramethylsilane. *J. Electron. Microsc.* **1994**, *43*, 111−115.
(58) Dey, S.; Baul, T. B.; Roy, B.; Dey, D. A New Rapid Method of Air-Drying for Scanning Electron Microscopy Using Tetramethylsilane. *J. Microsc.* **1989**, *156* (2), 259−261.
(59) Ilavsky, J. Nika: Software for Two-Dimensional Data Reduction. *J. Appl. Crystallogr.* **2012**, *45* (2), 324−328.
(60) Ilavsky, J.; Jemian, P. R. Irena: Tool Suite for Modeling and Analysis of Small-Angle Scattering. *J. Appl. Crystallogr.* **2009**, *42* (2), 347−353.

https://dx.doi.org/10.1021/acsnano.0c06389
ACS Nano 2020, 14, 17018−17027